

Article

# Highly Selective Tilted Triangular Springs with Constant Force Reaction †

Lisa Schmitt \* , Philip Schmitt  and Martin Hoffmann 

Microsystems Technology, Faculty of Electrical Engineering and Information Technology, Ruhr University Bochum, 44801 Bochum, Germany; philip.schmitt@rub.de (P.S.); martin.hoffmann-mst@rub.de (M.H.)

\* Correspondence: lisa.schmitt-mst@rub.de; Tel.: +49-(0)-234-32-24830

† This is an expanded research article based on the conference paper “Tilted Triangular Springs with Constant Force Reaction” that was presented at EUROSENSORS2023 conference, 10–13 September 2023 in Lecce, Italy.

**Abstract:** Guiding mechanisms are among the most elementary components of MEMS. Usually, a spring is required to be compliant in only one direction and stiff in all other directions. We introduce triangular springs with a preset tilting angle. The tilting angle lowers the reaction force and implements a constant reaction force. We show the influence of the tilting angle on the reaction force, on the spring stiffness and spring selectivity. Furthermore, we investigate the influence of the different spring geometry parameters on the spring reaction force. We experimentally show tilted triangular springs exhibiting constant force reactions in a large deflection range and a comb-drive actuator guided by tilted triangular springs.

**Keywords:** micromechanical spring; constant force mechanism; MEMS; electrostatic actuator

## 1. Introduction

Guiding mechanisms enable translational in-plane displacement of Micro-Electro-Mechanical Systems (MEMS) and are, therefore, among the most important components of microsystems technology. In MEMS, linear guiding mechanisms are used in a wide variety of applications such as in electrostatic actuators [1], or in inertial MEMS to guide proof masses. Usually, these applications require a guiding mechanism that is compliant in the displacement direction and stiff in all other directions. For a solid spring, this means that it should have a low stiffness,  $k_x$ , in the deflection direction,  $x$  (i.e., the slope of the force–displacement characteristic (FDC)), but high stiffnesses in the orthogonal  $y$ -direction ( $k_y$ ). The ratio of the stiffness can be defined as the selectivity,  $S$ , with

$$S = \frac{k_y}{k_x} \Big|_{y \rightarrow 0} \quad (1)$$

Guiding mechanisms have many different forms of appearance and geometries. We give a comprehensive overview of the guiding mechanisms in [2]. The clamped–clamped beams are among the most common guiding mechanisms [1,3] that fit the requirements for guiding springs quite well, as their stiffness in the displacement direction,  $k_x$ , is much smaller than their stiffness in the direction orthogonal to the displacement,  $k_y$ . Figure 1a shows a clamped–clamped beam and its typical non-linear FDC [4]. Consequently, the mechanical reaction force,  $F_x$ , of the clamped beams increases strongly with progressing displacement. This characteristic is quite unattractive for, e.g., electrostatic actuators. Serpentine springs have a linear FDC, as shown in Figure 1b; hence the mechanical force,  $F_x$ , increases only slightly during deflection, making the serpentine springs attractive for electrostatic comb-drive actuation [1,5]. However, serpentine springs only realize a uni-directional displacement and suffer from a strongly decreasing selectivity with progressing displacement that results, e.g., in the side instability of comb-drive actuators [1].



**Citation:** Schmitt, L.; Schmitt, P.; Hoffmann, M. Highly Selective Tilted Triangular Springs with Constant Force Reaction. *Sensors* **2024**, *24*, 1677. <https://doi.org/10.3390/s24051677>

Academic Editors: Bruno Ando, Pietro Siciliano and Luca Francioso

Received: 29 January 2024

Revised: 22 February 2024

Accepted: 29 February 2024

Published: 5 March 2024



**Copyright:** © 2024 by the authors. Licensee MDPI, Basel, Switzerland. This article is an open access article distributed under the terms and conditions of the Creative Commons Attribution (CC BY) license (<https://creativecommons.org/licenses/by/4.0/>).

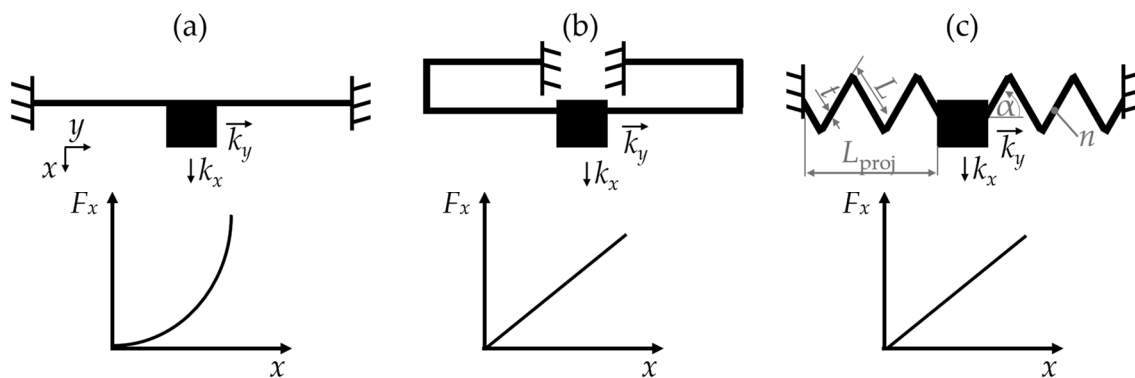


**Figure 1.** A sketch of the FDC of a (a) clamped–clamped beam, (b) serpentine spring, (c) triangular spring [2,3].

Springs with an M-shaped geometry have a non-linear and asymmetric FDC [6]. Both triangular and sinusoidal springs, presented in [2], have a geometry similar to the M-shaped springs. The triangular springs (Figure 1c) are characterized by a linear FDC, high selectivity, and a large displacement range. They achieve large deflections without rupture and can be deflected in both the positive and negative  $x$ -directions. The appearance of these springs is highly variable, since the number of spring segments  $n$ , the angle of inclination  $\alpha$  as well as the thickness,  $t$ , and the length,  $L$ , can be varied. The triangular springs can be migrated into sinusoidal shaped springs, which reduces the stress peaks that occur in the spring kinks and limits the maximum deflection of the spring [2].

There are also springs with a constant FDC [7]. The springs realize a constant force feedback when applying an external force, e.g., a voltage [8,9]. Consequently, the resulting force is not proportional to the deflection [9]. In the constant force range, the stiffness,  $k_x$ , of such springs is ideally 0 N/m. Constant-force springs are either used to maintain the functionality of sensitive MEMS, which could be affected by fluctuations of the spring force [10] or for specific applications that require a constant force [11]. A constant force can be accomplished by complex force feedback systems that control the force by means of an actuator [12,13]. To generate constant forces in microsystems, electrostatic actuators with closed-loop feedback control are often used to control the force in MEMS [14]. Alternatively, the spring itself can be used to generate a constant and displacement-independent force. Such systems include, for example, buckling beams combined with a linear spring [8,11,15]. Here, the FDC of the negative buckling spring is superimposed with the FDC of the linear spring. The superposition of both springs results in a displacement independent constant force reaction [11,16–19].

In this contribution, we present a tilted triangular shaped spring achieving constant force reactions. Unlike other solutions, the tilted triangular spring does not require a superimposing of multiple individual reaction forces making it a simple and compact solution for a linear guidance with a constant force. In Section 2, we present the spring design and discuss the simulation results. Here, we take a close look at the influence of the design parameters on the constant force range. In Section 3, we present the experimental setup and discuss the results obtained by the experiments. In Section 4, we show a comb-drive actuator displaced by a tilted triangular spring. Section 5 gives a short summary of this article.

## 2. Materials and Methods

### 2.1. Spring Design

The tilted triangular spring is characterized by a tilting angle,  $\beta$ , as shown in Figure 2a. The properties of this spring are defined by the number of straight elements,  $n$ , their length,  $L$ , the thickness,  $t$ , depth,  $d$ , of the device layer, and the inclination angle,  $\alpha$ . Figure 2 also shows the projected length,  $L_{\text{proj}}$ . Based on the results that we achieved in [2], we aim to achieve symmetrical force-displacement curves. Therefore, we only used springs with an

even number of beams, i.e.,  $n = 2, 4, 6, \dots$ , and the length of the first,  $L_1$ , and the last beam,  $L_n$ , is half the length of the other beams, i.e.,  $L/2$ . The triangular spring achieves a constant force reaction with a preset initial tilting angle,  $\beta$ , as an additional degree of freedom. To realize a translational displacement, we use a symmetric design (Figure 2b). As shown in Figure 2b, the constant force range (CFR) arises with the progressing displacement of the spring; consequently, the tilted triangular spring achieves a partially constant spring force.

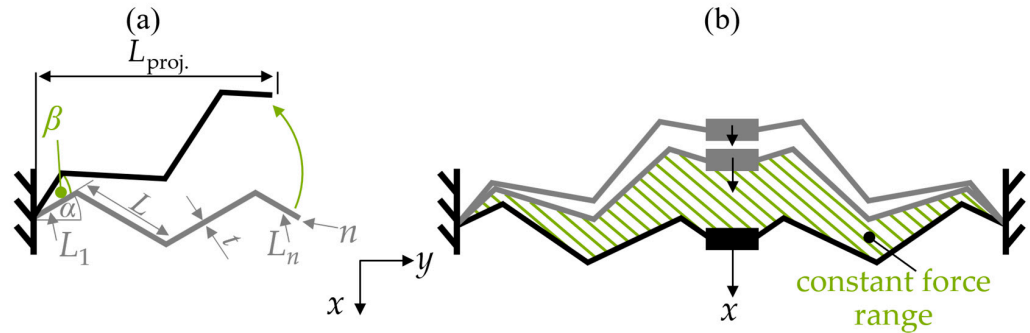


**Figure 2.** (a) A sketch of the tilted triangular spring with a preset tilting angle,  $\beta$ , (b) displacement of the tilted triangular spring with a constant force region.

## 2.2. Simulation Procedure

The springs are simulated by FEM using COMSOL *Multiphysics*. We simulate a system with four identical springs with identical design parameters (Figure 3) to guarantee a translational displacement and to maintain the system stability. The structures are simulated with respect to the geometric non-linearity.

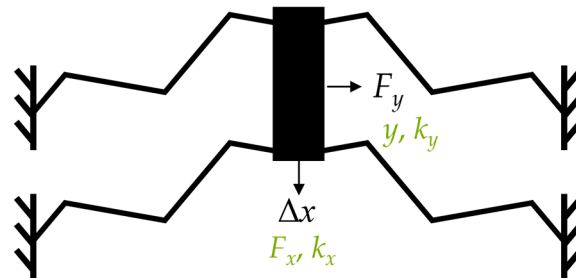


**Figure 3.** Simulation setup; applied force or displacement (black); resulting values (green).

The springs are displaced in defined steps,  $\Delta x$ , resulting in a change in the mechanical reaction force of the spring,  $\Delta F_x$ . With

$$k_x = \frac{\Delta F_x}{\Delta x} \quad (2)$$

we determine the stiffness,  $k_x$ , in the displacement direction. In a second simulation, a constant force,  $F_y$ , also acts in the  $y$ -direction, resulting in a displacement,  $y$ . With

$$k_y = \frac{F_y}{y} \quad (3)$$

we determine the stiffness,  $k_y$ , of the spring when displaced in the  $x$ -direction. The selectivity,  $S$ , of the spring is given by (1) as the quotient of  $k_y$  and  $k_x$ .

The design parameters are given in Table 1. To analyze the influence of the tilting angle on the reaction force, stiffness, and selectivity, we designed triangular springs with the ability to vary the tilting angle,  $\beta$ , from  $0^\circ$  to  $8^\circ$  as shown in Figures 4 and 5. To analyze the correlation between the position of the maximum selectivity,  $x(S_{\max})$ , the projected length,  $L_{\text{proj}}$ , and the tilting angle, the tilting and inclination angle, as well as the number

of beams were varied in Figure 5b. In Figure 6, the influence of the design parameters was investigated. Therefore, in each diagram, one single parameter was varied and the influence on the constant force range was analyzed.

**Table 1.** Parameters of simulated triangular-shaped springs; the varied parameters are in bold.

Analyzed in	$\beta$	$\alpha$	$n$	$L$	$t$	$d$	Analysis of
Figure 4a–c	<b>0–8°</b>	20°	6	400 $\mu\text{m}$	5 $\mu\text{m}$	20 $\mu\text{m}$	reaction force $F_x$ , stiffness $k_x$ and $k_y$
Figure 5a	<b>0–8°</b>	20°	6	400 $\mu\text{m}$	5 $\mu\text{m}$	20 $\mu\text{m}$	selectivity $S$
Figure 5b	<b>0°–8°</b>	<b>10°, 20°, 30°</b>	<b>4, 6</b>	400 $\mu\text{m}$	5 $\mu\text{m}$	20 $\mu\text{m}$	correlation $S_{\max}$ , $L_{\text{proj}}$ and $\beta$
<b>Figure 6a standard spring</b>	<b>7°</b>	<b>20°</b>	<b>6</b>	<b>400 <math>\mu\text{m}</math></b>	<b>5 <math>\mu\text{m}</math></b>	<b>20 <math>\mu\text{m}</math></b>	<b>constant force</b>
Figure 6b	<b>0–30°</b>	20°	6	400 $\mu\text{m}$	5 $\mu\text{m}$	20 $\mu\text{m}$	Influence of $\beta$
Figure 6c	7°	<b>5–30°</b>	6	400 $\mu\text{m}$	5 $\mu\text{m}$	20 $\mu\text{m}$	Influence of $\alpha$
Figure 6d	7°	20°	<b>4–14</b>	400 $\mu\text{m}$	5 $\mu\text{m}$	20 $\mu\text{m}$	Influence of $n$
Figure 6e	7°	20°	6	<b>100...500 <math>\mu\text{m}</math></b>	5 $\mu\text{m}$	20 $\mu\text{m}$	Influence of $L$
Figure 6f	7°	20°	6	400 $\mu\text{m}$	<b>3...10 <math>\mu\text{m}</math></b>	20 $\mu\text{m}$	Influence of $t$

### 2.3. Simulation Results

#### 2.3.1. Constant Force Range (CFR) and Selectivity

Figure 4a shows the simulated force reaction of a triangular spring for different preset tilting angles  $\beta$ . For tilting angles from 0° to 5°, the reaction force increases continuously. For tilting angles of 6° and 7°, the spring exhibits an approximately constant force range. For the selected geometry, the force reaction shows local maxima and minima for a tilting angle  $\beta = 8^\circ$  or higher.

Figure 4b shows the resulting spring stiffness,  $k_x$ , in the displacement direction,  $x$ . For the springs with constant force reaction ( $\beta = 6^\circ$  and  $7^\circ$ ), the stiffness is approx. 0 N/m in the CFR. As shown in Figure 4c, the stiffness orthogonal to the displacement,  $k_y$ , slightly increases for springs with no or small tilting angles, whereas springs with larger tilting angles have a slightly decreasing stiffness,  $k_y$ .

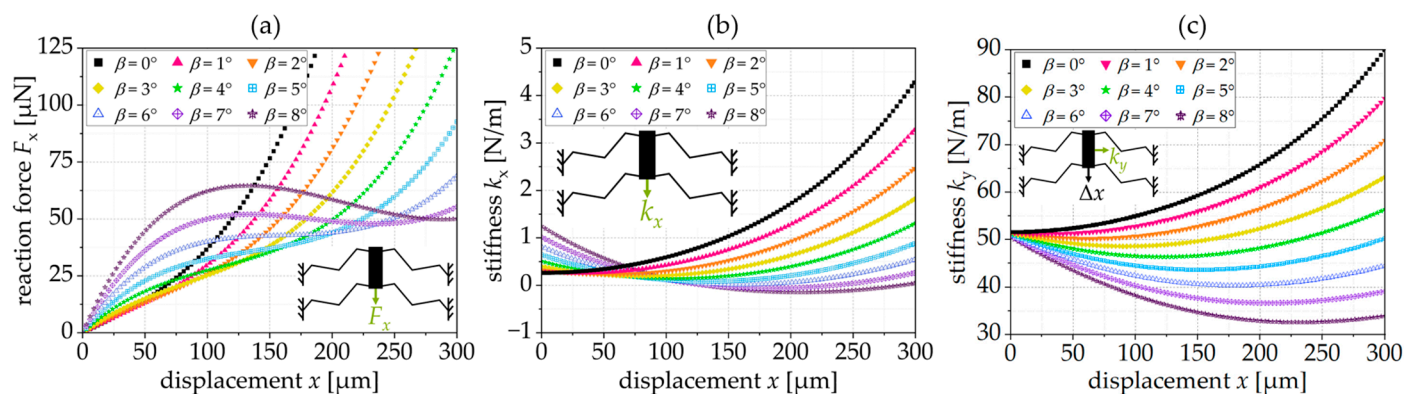


**Figure 4.** (a) Reaction force,  $F_x$ , as a function of  $\beta$ , (b) stiffness,  $k_x$ , as a function of  $\beta$ , (c) stiffness,  $k_y$ , as a function of  $\beta$ ; simulation results for an exemplary spring with  $L = 400 \mu\text{m}$ ,  $t = 5 \mu\text{m}$ ,  $n = 6$  and  $\alpha = 20^\circ$ .

Figure 5a shows the resulting selectivity,  $S$ . Apart from generating a constant force, tilted triangular springs exhibit a high level of selectivity, as defined by the stiffness ratio between the  $y$ - and  $x$ -directions (cf. (1)). With the increase in the tilting angle, the maximum

selectivity,  $S_{\max}$ , increases, too. Consequently, the tilted triangular spring exhibits a selectivity,  $S$ , as a function of the tilting angle. Thereby, the position of the maximum selectivity,  $x(S_{\max})$ , shifts towards larger displacements. Springs with a reaction force featuring a local maximum and minimum do not have a defined maximum of selectivity. The increase in selectivity is important, e.g., for the lateral instability of the comb-drive actuators. A higher selectivity allows a higher voltage,  $U_{SI}$ , to be applied, and thus allows larger displacements before lateral-side instability occurs. This correlation results from the analytical model for the displacement of comb-drive actuators that is highly dependent on the selectivity,  $S$ , [1].

$$U_{SI}^2 = \frac{b^2 k_x}{2\epsilon_0 \epsilon_r d n_e} \left( \sqrt{2 \frac{k_y}{k_x} + \frac{x_0^2}{b^2}} - \frac{x_0}{b} \right) = \frac{b^2 k_x}{2\epsilon_0 \epsilon_r d n_e} \left( \sqrt{2S + \frac{x_0^2}{b^2}} - \frac{x_0}{b} \right) \quad (4)$$

Here,  $U_{SI}$  is the voltage when side instability occurs,  $b$  is the distance between two electrodes,  $n_e$  is the number of electrodes,  $d$  is the thickness of the device layer, and  $x_0$  is the initial overlap of electrodes.

Figure 5b shows that the position of maximum selectivity normalized to the projected spring length,  $L_{proj}$ , depends only on the tilting angle,  $\beta$ , and increases almost linearly with it. Consequently, a spring with a tilting angle of, e.g.,  $\beta = 6^\circ$  reaches its maximum selectivity at a deflection of about 4.5% of its projected length.

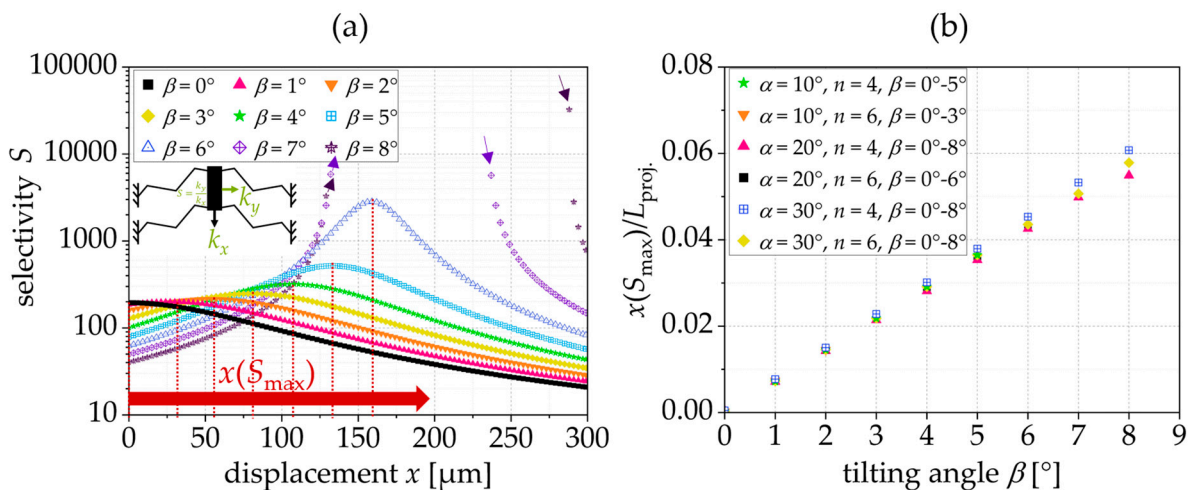


**Figure 5.** (a) Selectivity,  $S$ , as a function of  $\beta$ ; (b) position of maximum selectivity,  $x(S_{\max})$ , normalized to  $L_{proj}$ , depending on the tilting angle,  $\beta$ ; simulation results for an exemplary spring with  $L = 400 \mu\text{m}$  and  $t = 5 \mu\text{m}$ .

### 2.3.2. Influence of the Spring Parameter on the Constant Force Range

To better analyze the influence of the different geometry parameters of the tilted triangular spring on the constant force reaction, we use a standard spring with a force reaction, as shown in Figure 6a, with a constant force of  $50.1 \pm 1.5 \mu\text{N}$  in the range of  $100 \mu\text{m}$  to  $250 \mu\text{m}$ . In Figure 6b–f, we vary a single geometry parameter.

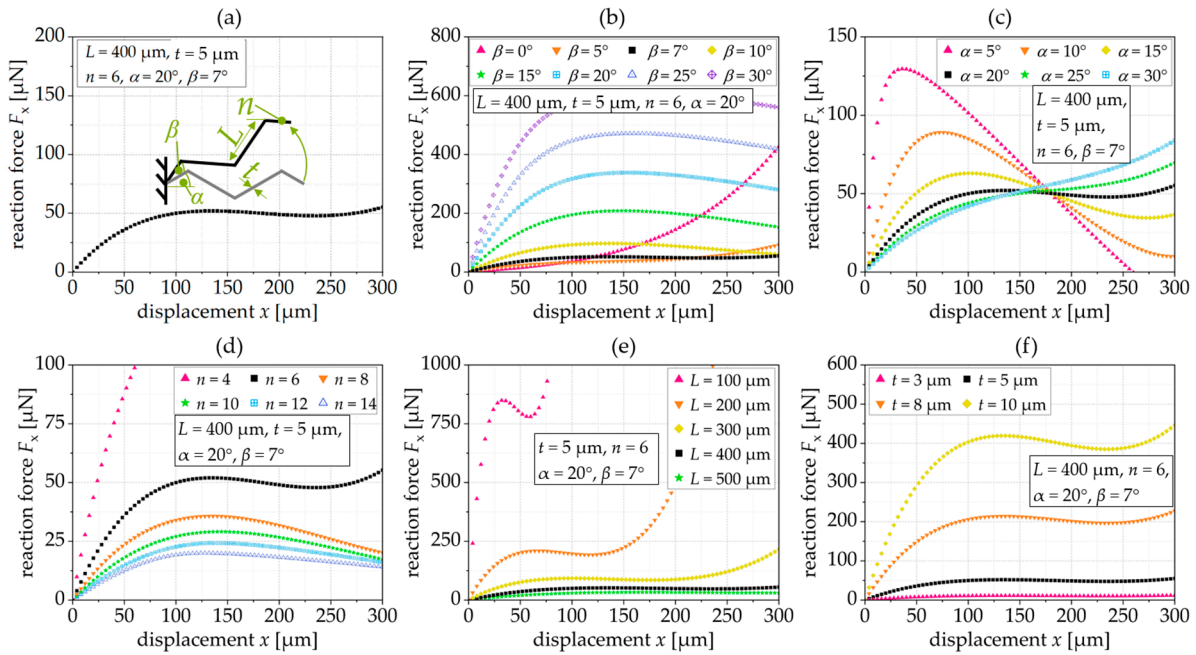
Figure 6b shows the influence of the tilting angle,  $\beta$ , on the constant force. At small tilting angles (in this case,  $\beta = 5^\circ$ ), no constant force range is achieved, while at larger tilting angles, the force response decreases slightly (negative stiffness) after reaching a maximum.

Figure 6c shows the influence of the inclination angle,  $\alpha$ , which in this case defines the constant force range at  $20^\circ$ . If the inclination angle decreases, the reaction force increases sharply before it drops sharply. For a larger  $\alpha$  (here,  $\alpha = 30^\circ$ ), the reaction force increases with increasing deflection without establishing an extended constant force range.

Figure 6d shows the influence of the number of beam segments,  $n$ . If the spring consists of few beam segments, in this case  $n = 4$ , there is no constant force; if there are many beam segments, the reaction force decreases after reaching a maximum.

Figure 6e shows that springs with long segments have a low reaction force and a large linear force range. If the segments of the tilted triangular spring are short, in this case 100  $\mu\text{m}$  and 200  $\mu\text{m}$ , respectively, the spring force is higher and the constant force range is non-existent or very small.

The segment thickness,  $t$ , is used to set the level of the reaction force, so that as the thickness decreases, the reaction force decreases and the constant force range increases, as shown in Figure 6f.



**Figure 6.** Simulated force–displacement characteristic of (a) a standard spring ( $L = 400 \mu\text{m}$ ,  $t = 5 \mu\text{m}$ ,  $n = 6$ ,  $\beta = 7^\circ$  and  $\alpha = 20^\circ$ ), when varying (b) the tilting angle,  $\beta$ , (c) the inclination angle,  $\alpha$ , (d) the number of beams,  $n$ , (e) the beam length,  $L$ , (f) the beam thickness,  $t$ .

The optimal design depends on the application and the design of interacting components on the chip. The design can be optimized to, e.g., a large constant force range, a very high or very low constant force, or a spring with a small length or height. An example of this is as follows: (1) If a large constant force range is required, it is useful to have a long beam length,  $L$ , or thin beam thickness,  $t$ . However, large beams require a lot of space, and the beam thickness can be limited by the quality of the etching process or the thickness of the device layer. (2) If a constant and high reaction force is required, the tilting angle or the thickness can be increased. However, a spring with a high tilting angle requires lots of space. Consequently, the optimal design always depends on the application, other chips' design properties or the etching processes, and we cannot derive a single expression for an optimal spring design.

#### 2.4. Fabrication

Based on the simulations conducted, demonstrator springs were designed. In addition to that, an electrostatic comb-drive actuator was designed to provide the tilted springs with a constant force.

The chips were manufactured in a dicing-free process for silicon-on-insulator (SOI) substrates known from [20] using a device layer of 20  $\mu\text{m}$  and a handle layer of 300  $\mu\text{m}$ ; this is shown in Figure 7. First, a 100 nm aluminum layer was sputtered on the device layer. The aluminum was used for the electrostatic activation of the comb-drive electrodes. Afterwards, the electrical contacts were patterned by lithography and wet chemical etching, so that the mechanical structures were not covered with aluminum (Figure 7a). In the next step, we etched the handle layer by deep reactive ion etching (DRIE) using a  $\text{SiO}_2$ -hard

mask (Figure 7b). To structure the device layer, we used a hard mask of aluminum nitride (AlN) and DRIE (Figure 7c). The chips were released from the substrate by hydrofluoric vapor etching (Figure 7d). Afterwards, the chips were fixed on PCBs. The simulated thickness of the springs was 5  $\mu\text{m}$ ; however, the fabricated thickness was 4.8  $\mu\text{m}$ . Figure 7e shows a stacking photo of a fabricated chip with the spring demonstrator. Each spring system consists of a slider with two tilted guiding springs on each side. We provided the springs with additional force sensors to experimentally determine the force reaction on-chip. The chips also contain reference force sensors to determine the stiffness of the force sensors.

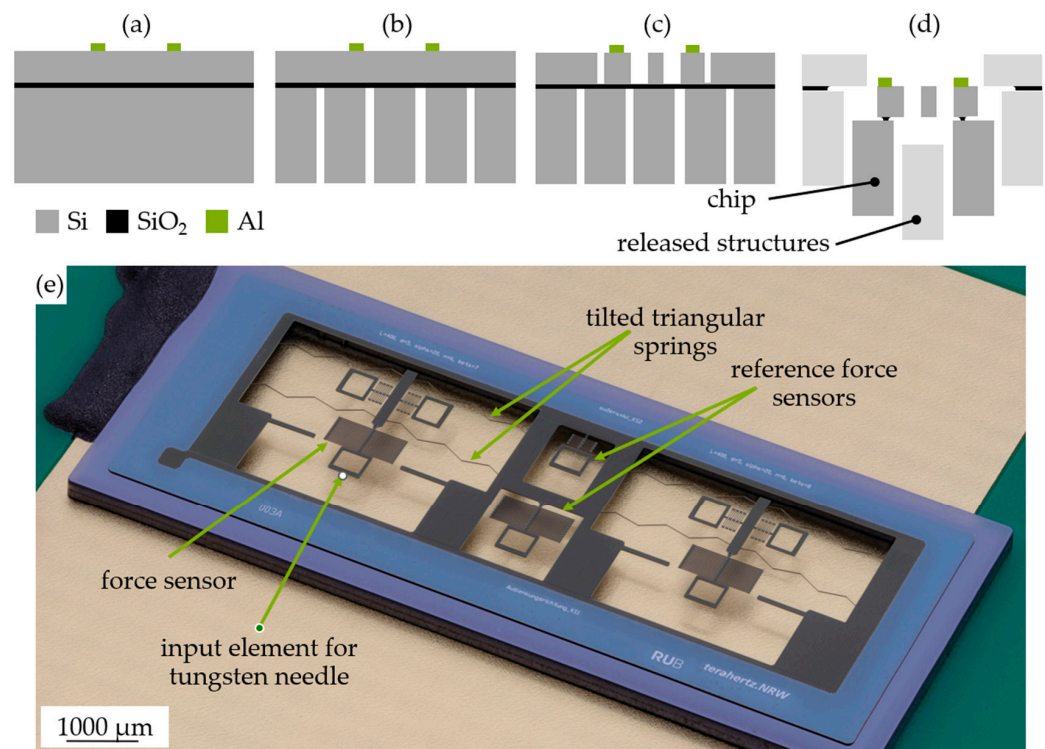


**Figure 7.** (a–d) Fabrication flowchart, (e) stacking photo of the fabricated chip.

### 2.5. Experimental Characterization Procedure

First, the integrated force sensors were calibrated. Therefore, we could determine the spring constant,  $k_{\text{FS}}$ , of the force sensor. Instead of using the springs that were already connected to the tested device, we used the reference force sensors shown in Figure 7e. The calibration procedure included the simultaneous measurement of force and displacement of the force sensor, as illustrated in Figure 8a. The chips were mounted on a piezoelectric stage (PI Q-545). A tungsten needle was inserted into the input element of the reference force sensor. This needle was connected to a load cell (Sartorius WZA224-ND) with a resolution of 0.1  $\mu\text{N}$ . The piezo stage was shifted upwards stepwise in defined increments. This resulted in an expansion of the force sensor and changed the force reaction measured by the load cell. Using (2), the spring constants of the reference force sensors were measured to be 0.2 N/m for force sensor 1 and 0.55 N/m, 1.5 N/m, and 4.6 N/m for force sensors 2, 3, and 4, respectively.

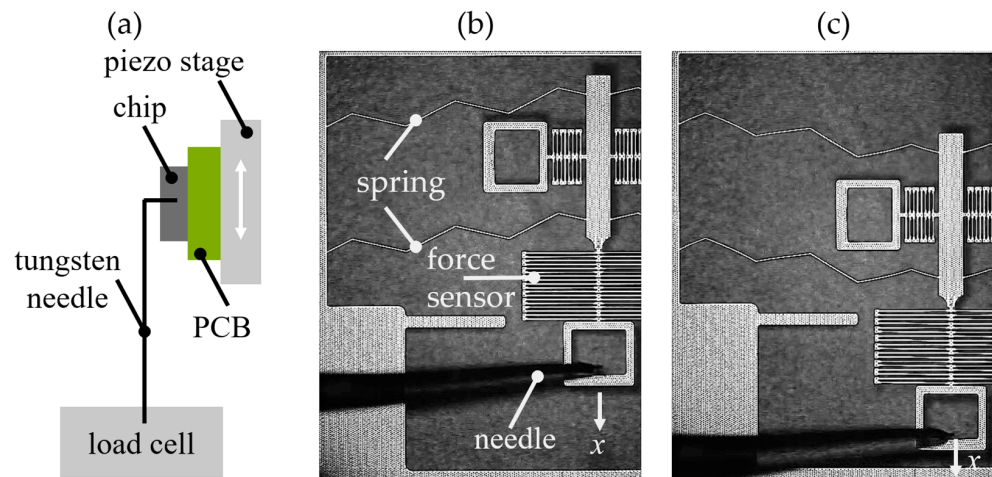


**Figure 8.** (a) sketch of the setup for calibrating the force sensor; left-hand-side of the tilted triangular spring in (b) the initial position, and (c) the displaced spring.

Knowing the spring constant of the force sensor, the triangular springs could be characterized using the integrated force sensors on the device under test. Therefore, again, a needle was connected to the input element of the force sensor and a displacement controlled by a piezo stage was imposed at the spring, as shown in Figure 8b. Both the deflection of the slider and the extension of the force sensor were measured visually with a microscope camera. With

$$F_{\text{DUT}}(x) = F_{\text{FS}}(x) = k_{\text{FS}}x \quad (5)$$

the force was measured as a function of the spring displacement, which yielded the FDC. A deflected spring is shown in Figure 8c. Each experiment was repeated three times and the mean values and a standard deviation were calculated.

### 3. Experimental Results and Discussion

#### 3.1. Overview of the Results

Table 2 summarizes the parameters of the selected spring designs.

**Table 2.** Parameters of selected spring designs.

Analyzed in	$\beta$ [°]	$\alpha$ [°]	$n$	$L$ [μm]	$t$ [μm]	$d$ [μm]	$F_{x,\text{konst.}} (\text{exp.})$	$F_{\text{konst., range}} (\text{exp.})$
Figure 9	0, 2, 4, 6, 7, 8, 10	20	6	400	4.8	20	$6.8 \pm 0.3 \mu\text{N}$ ( $\beta = 7^\circ$ )	$97 \dots 267 \mu\text{m}$ ( $\beta = 7^\circ$ )
Figure 10a	0, 8, 9, 10, 11	30	6	400	4.8	20	$6.4 \pm 1.1 \mu\text{N}$ ( $\beta = 10^\circ$ )	$105 \dots 355 \mu\text{m}$ ( $\beta = 10^\circ$ )
Figure 10b	7	20	6	400	4.8, 9.4, 14.8, 19.7	20	$147.4 \pm 1.1 \mu\text{N}$ ( $t = 9.4 \mu\text{m}$ )	$103 \dots 228 \mu\text{m}$ ( $t = 9.4 \mu\text{m}$ )
Figure 10c	7	20	6	400, 600	4.8	20	$4.1 \pm 0.3 \mu\text{N}$ ( $L = 600 \mu\text{m}$ )	$74 \dots 324 \mu\text{m}$ ( $L = 600 \mu\text{m}$ )

#### 3.2. Characterization of the Tilted Triangular Springs

We designed triangular springs where the tilting angle varied from  $0^\circ$  to  $8^\circ$ . The design parameters of the spring are given in Table 2.

Figure 9a shows the experimentally derived reaction force depending on the tilting angle  $\beta$ . As shown in the simulation results, a constant force appears within the span of  $\beta = 6^\circ$  to  $\beta = 8^\circ$ . For  $\beta = 10^\circ$ , and the force reaction curve has a local maximum. The experimentally derived reaction force ( $6.8 \pm 0.3 \mu\text{N}$  for  $\beta = 7^\circ$ ) is smaller than the simulated reaction force, which correlates to the smaller thickness of the fabricated springs (see Section 2.3). However, the region with the constant force is also larger, e.g., for  $\beta = 7^\circ$ , the

CFR starts with a displacement of 97  $\mu\text{m}$  and ends at 267  $\mu\text{m}$ . Figure 9b shows the resulting spring stiffness for exemplary springs that is close to 0 N/m for the constant force range of the springs with a tilting angle of 7° and 8°.

Comparing the experimental results with the simulation presented in Figure 4a, the reaction force is lower, which is attributed to the reduced thickness of the manufactured structures ( $t = 4.8 \mu\text{m}$  (fabrication) instead of  $t = 5.0 \mu\text{m}$  (simulation)). This is because the thickness,  $t$ , of the springs has a cubic influence on the reaction force. The manufactured springs show a lower increase in the reaction force and a smaller influence of the tilting angle on the constant force range. In Figure 4a, the simulated springs with a tilting angle of 4° and 8° do not show a constant force range, while the fabricated springs with these tilting angles show a constant force behavior in Figure 9a.

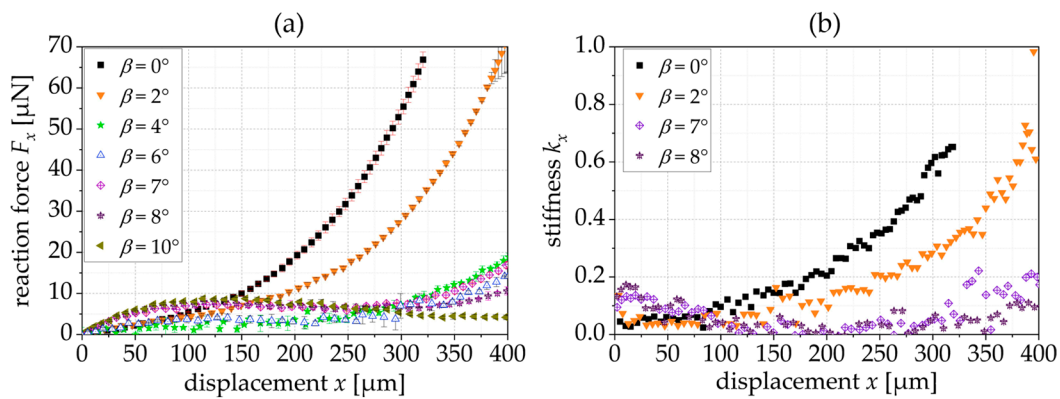


**Figure 9.** (a) Experimentally derived FDC of triangular springs when varying the tilting angle  $\beta$ ; (b) resulting stiffness  $k_x$  ( $L = 400 \mu\text{m}$ ,  $t = 4.8 \mu\text{m}$ ,  $n = 6$  and  $\alpha = 20^\circ$ ).

As shown in Figure 6c, the inclination angle,  $\alpha$ , also influences the reaction force. In Figure 10a, we show the corresponding experimental results for a spring with an inclination angle  $\alpha = 30^\circ$ . To generate a constant force, we need a larger tilting angle when the inclination angle is higher. Figure 10b shows the influence of the spring thickness,  $t$ , on the reaction force. The reaction force increases with increasing thickness. Thereby, the CFR is becoming smaller. Figure 8c shows that the larger beam segments also achieve larger constant force regions with a slightly smaller reaction force.

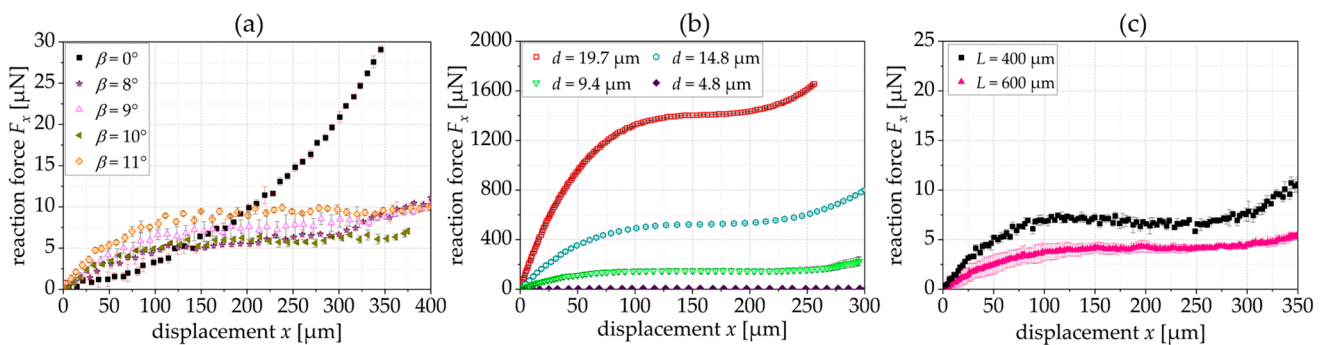


**Figure 10.** (a) Experimentally derived FDC of triangular springs when varying the tilting angle,  $\beta$ , ( $\alpha = 30^\circ$ ); (b) experimentally shown influence of the spring thickness,  $t$ , on the reaction force; (c) experimentally shown influence of the beam length,  $L$ , on the reaction force.

#### 4. Application in Comb Drive Actuators

An application for the presented springs are comb-drive actuators that struggle with side instability, which means that electrodes guided by the spring escape to the mounted electrodes, limiting the displacement of the comb-drive actuator (cf. Section 2.3). This

happens as soon as the first derivative of the electrostatic force with respect to  $y$  becomes larger than the restoring spring constant in the  $y$ -direction [1].

We use the spring characterized in Figure 9 with a tilting angle of  $\beta = 7^\circ$  to guide an electrostatic comb-drive actuator. Figure 11a shows a schematic of the setup of the actuator; Figure 11b shows the voltage-dependent displacement with a relatively large displacement at low voltage. The maximum displacement is  $71 \mu\text{m}$  at  $28 \text{ V}$ , and at larger voltages, side instability occurs. Figure 11c,d show the displacing electrodes.

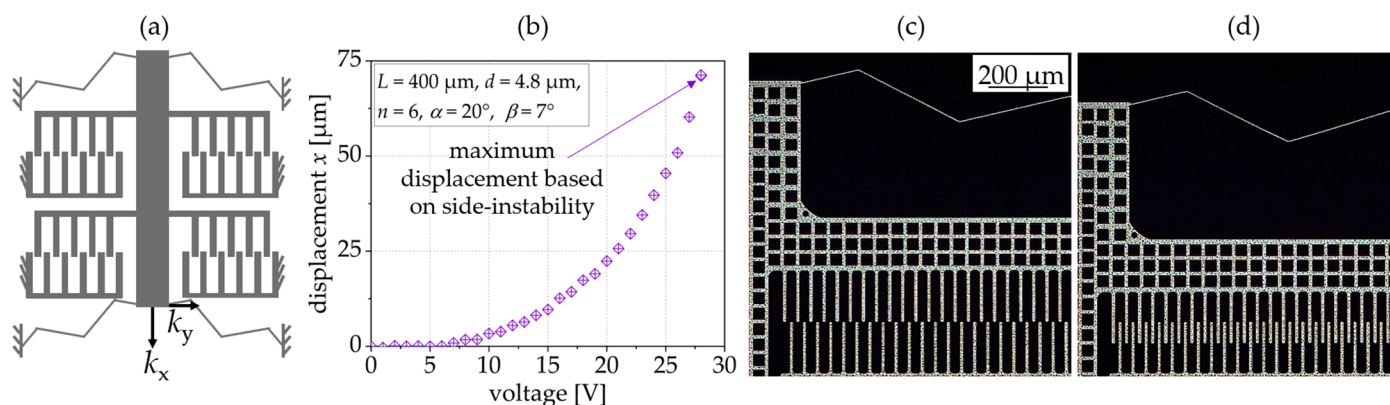


**Figure 11.** (a) sketch of the actuator setup; (b) experimentally derived voltage-displacement characteristics of a comb-drive actuator guided by the tilted triangular spring presented in Figure 7 ( $\beta = 7^\circ$ ); comb-drive actuator at (c)  $0 \text{ V}$  and (d)  $28 \text{ V}$ .

## 5. Conclusions

In this contribution, we present tilted triangular springs that achieve a partially constant reaction force using a preset tilting angle,  $\beta$ . Constant force springs are suitable for mechanisms which control an object with a defined force, as well as for all MEMS in which a mechanical overload could lead to a functional restriction or destruction of the sensitive components. Here, we focus on the influence of the different geometry parameters on the spring reaction force and analyze the spring selectivity based on the tilting angle. An exemplary spring achieves a constant force of  $6.8 \pm 0.3 \mu\text{N}$  in the range of  $97 \mu\text{m}$  to  $267 \mu\text{m}$ . We show that tilted triangular springs are very well-suited for guiding large displacement comb-drive actuators due to their high selectivity.

**Author Contributions:** Conceptualization, L.S. and P.S.; methodology, L.S. and P.S.; software, L.S. and P.S.; validation, L.S. and P.S.; formal analysis, L.S.; investigation, L.S.; resources, M.H.; data curation, L.S.; writing—original draft preparation, L.S.; writing—review and editing, P.S. and M.H.; visualization, L.S.; supervision, P.S. and M.H.; project administration, M.H.; funding acquisition, M.H. All authors have read and agreed to the published version of the manuscript.

**Funding:** This research was partly funded by the project terahertz.NRW. The project “terahertz.NRW” is receiving funding from the programme “Netzwerke 2021” (NW21-068D), an initiative of the Ministry of Culture and Science of the State of Northrhine Westphalia. The sole responsibility for the content of this publication lies with the authors. This research was also partly funded by the Deutsche Forschungsgemeinschaft (DFG, German Research Foundation)—Project-ID 287022738—TRR 196, Project C12.

**Institutional Review Board Statement:** Not applicable.

**Informed Consent Statement:** Not applicable.

**Data Availability Statement:** The data can be provided by L.S. upon reasonable request.

**Acknowledgments:** The chips were partly fabricated at the ZGH, Ruhr-Universität Bochum. The authors thank the technical staff of the Microsystems Technology (MST) for the support in the cleanroom.

**Conflicts of Interest:** The authors declare no conflicts of interest.

## References

1. Legtenberg, R.; Groeneveld, A.W.; Elwenspoek, M. Comb-drive actuators for large displacements. *J. Micromech. Microeng.* **1996**, *6*, 320. [[CrossRef](#)]
2. Schmitt, P.; Schmitt, L.; Tsivin, N.; Hoffmann, M. Highly Selective Guiding Springs for Large Displacements in Surface MEMS. *J. Microelectromech. Syst.* **2021**, *30*, 597–611. [[CrossRef](#)]
3. Schomburg, W.K. *Introduction to Microsystem Design*; Springer: Berlin, Germany, 2011.
4. Gao, Y.; You, Z.; Zhao, J. Electrostatic comb-drive actuator for MEMS relays/switches with double-tilt comb fingers and tilted parallelogram beams. *J. Micromech. Microeng.* **2015**, *25*, 45003. [[CrossRef](#)]
5. Schmitt, L.; Conrad, P.; Kopp, A.; Ament, C.; Hoffmann, M. Non-Inchworm Electrostatic Cooperative Micro-Stepper-Actuator Systems with Long Stroke. *Actuators* **2023**, *12*, 150. [[CrossRef](#)]
6. Leadenham, S.; Erturk, A. M-shaped asymmetric nonlinear oscillator for broadband vibration energy harvesting: Harmonic balance analysis and experimental validation. *J. Sound Vib.* **2014**, *333*, 6209–6223. [[CrossRef](#)]
7. Imorkvenaitė-Vilkonciene; Bucinskas, V.; Subaciute-Zemaitiene, J.; Sutinytis, E.; Virzonis, D.; Dzedzickis, A. Development of Electrostatic Microactuators: 5-Year Progress in Modeling, Design, and Applications. *Micromachines* **2022**, *13*, 1256. [[CrossRef](#)] [[PubMed](#)]
8. Wang, P.; Xu, Q. Design and modeling of constant-force mechanisms: A survey. *Mech. Mach. Theory* **2018**, *119*, 1–21. [[CrossRef](#)]
9. Yang, S.; Xu, Q. Design and simulation of a passive-type constant-force MEMS microgripper. In Proceedings of the 2017 IEEE International Conference on Robotics and Biomimetics (ROBIO), Macau, Macao, 5–8 December 2017; pp. 1100–1105.
10. Ma, C.; Du, J.; Liu, Y.; Chu, Y. Overview of micro-force sensing methods. *Appl. Mech. Mater.* **2014**, *462–463*, 25–31. [[CrossRef](#)]
11. Thewes, A.C.; Schmitt, P.; Löhler, P.; Hoffmann, M. Design and characterization of an electrostatic constant-force actuator based on a non-linear spring system. *Actuators* **2021**, *10*, 192. [[CrossRef](#)]
12. Li, B.; Li, G.; Lin, W.; Xu, P. Design and constant force control of a parallel polishing machine. In Proceedings of the 2014 4th IEEE International Conference on Information Science and Technology, Shenzhen, China, 26–28 April 2014; pp. 324–328.
13. Erlbacher, E. Method for Applying Constant Force with Nonlinear Feedback Control and Constant Force Device Using Same. U.S. Patent 5,448,146, 5 September 1995.
14. Boudaoud, M.; Haddab, Y.; Le Gor, Y. Modeling and optimal force control of a nonlinear electrostatic microgripper. *IEEE/ASME Trans. Mechatron.* **2012**, *18*, 1130–1139. [[CrossRef](#)]
15. Shahan, D.; Fulcher, B.; Seepersad, C.C. Robust design of negative stiffness elements fabricated by selective laser sintering. In Proceedings of the 2011 International Solid Freeform Fabrication Symposium, Austin, TX, USA, 11–14 August 2011; University of Texas at Austin: Austin, TX, USA, 2011.
16. Qiu, J.; Lang, J.H.; Slocum, A.H. A curved-beam bistable mechanism. *J. Microelectromech. Syst.* **2004**, *13*, 137–146. [[CrossRef](#)]
17. Qiu, J.; Lang, J.H.; Slocum, A.H. A centrally-clamped parallel-beam bistable MEMS mechanism. Technical Digest. In Proceedings of the MEMS 2001. 14th IEEE International Conference on Micro Electro Mechanical Systems (MEMS), Interlaken, Switzerland, 25 January 2001; pp. 353–356.
18. Vysotskyi, B.; Parrain, F.; Aubry, D.; Gaucher, P.; Le Roux, X.; Lefeuvre, E. Engineering the structural nonlinearity using multimodal-shaped springs in MEMS. *J. Microelectromech. Syst.* **2018**, *27*, 40–46. [[CrossRef](#)]
19. Vysotskyi, B.; Parrain, F.; Aubry, D.; Gaucher, P.; Lefeuvre, E. Innovative energy harvester design using bistable mechanism with compensational springs in gravity field. *Proc. J. Phys. Conf.* **2016**, *773*, 12064. [[CrossRef](#)]
20. Sari, I.; Zeimpekis, I.; Kraft, M. A dicing free SOI process for MEMS devices. *Microelectron. Eng.* **2012**, *95*, 121–129. [[CrossRef](#)]

**Disclaimer/Publisher's Note:** The statements, opinions and data contained in all publications are solely those of the individual author(s) and contributor(s) and not of MDPI and/or the editor(s). MDPI and/or the editor(s) disclaim responsibility for any injury to people or property resulting from any ideas, methods, instructions or products referred to in the content.